

# Global Spiral Density Wave Modes in Protoplanetary Disks: Morphology of Spiral Arms

ENZE CHEN <sup>1,2</sup> SI-YUE YU <sup>1,2</sup> AND LUIS C. HO <sup>1,2</sup>

<sup>1</sup>*Kavli Institute for Astronomy and Astrophysics, Peking University, Beijing 100871, China*

<sup>2</sup>*Department of Astronomy, School of Physics, Peking University, Beijing 100871, China*

## ABSTRACT

We analyze two-armed global spiral density wave modes generated by gravitational instability in razor-thin, non-viscous, self-gravitating protoplanetary disks to understand the dependence of spiral arm morphology (pitch angle  $\alpha$  and amplitude) on various disk conditions. The morphologies of the resulting spiral density wave modes closely resemble observations. Their pitch angles and pattern speeds are insensitive to the boundary conditions adopted. Gaussian disks exhibit more tightly wound spirals (smaller pitch angle) than power law disks under the same conditions. We find that at a fixed disk-to-star mass ratio ( $M_d/M_*$ ), pitch angle increases with average Toomre's stability parameter ( $\bar{Q}$ ) or average disk aspect ratio ( $\bar{h}$ ). For a given  $\bar{Q}$ , density wave modes with higher  $M_d/M_*$  have larger pitch angles, while the behavior reverses for a given  $\bar{h}$ . The interdependence between pitch angle and disk properties can be roughly approximated by  $\alpha \propto c_s^2/M_d$ , where  $c_s$  is the sound speed. Our gravitational instability-excited spiral density waves can be distinguished from planet-launched spirals: (1) massive cool disks have spiral pitch angle falling with radius, while low-mass hot disks have spiral pitch angle rising with radius; (2) the profile of spiral amplitude presents several dips and bumps. We propose that gravitational instability-excited density waves can serve as an alternative scenario to explain the observed spiral arms in self-gravitating protoplanetary disks.

*Keywords:* protoplanetary disks

## 1. INTRODUCTION

Substructures of protoplanetary disks, including cavities, gaps, rings, and spiral arms, have been revealed owing to detailed high-resolution observations (e.g., ALMA Partnership et al. 2015; Dong et al. 2018a; Huang et al. 2018). Spiral structure has been detected in protoplanetary disks in near-infrared scattered-light images that observe the disk surface (Hashimoto et al. 2011; Muto et al. 2012; Garufi et al. 2013; Grady et al. 2013; Wagner et al. 2015; Avenhaus et al. 2017; Benisty et al. 2017; Canovas et al. 2018; Uyama et al. 2018), in millimeter continuum images that probe the cold dust in the disk midplane (Pérez et al. 2016; Huang et al. 2018; Kurtovic et al. 2018), and in CO emission maps that detect the gas distribution (Tang et al. 2012; Huang et al. 2020). A significant fraction of observed spirals in protoplanetary disks are two-armed grand-design (e.g., Garufi et al.

2013; Benisty et al. 2017; Huang et al. 2018). Studies of the spiral arms and other substructures potentially help us understand the ongoing dynamic processes of protoplanetary disks (e.g., Dipierro et al. 2015; Dong et al. 2015a,b; Zhu et al. 2015).

Gravitational perturbation from embedded planets or nearby stars drives spiral arms in protoplanetary disks. An embedded planet is expected to launch a primary one-armed spiral wake (Goodman & Rafikov 2001; Rafikov 2002). A secondary or even a tertiary spiral arm interior to the planet orbit arises (Zhu et al. 2015; Miranda & Rafikov 2019), owing to constructive interference of different sets of density wave modes, with the arm number being dependent on the planet mass and disk temperature profile (Bae & Zhu 2018). Simulations of planet-disk interaction have produced planet-excited spiral wakes with appearance closely similar to observations (Dong et al. 2015b, 2016b; Fung & Dong 2015; Zhu et al. 2015). Meanwhile, two-armed spirals also can be launched by a nearby star, such as those seen in the HD 100453 system (Dong et al. 2016b; Wagner et al. 2018).

Another physical mechanism that can form spiral arms is gravitational instability (GI; e.g., Rice et al. 2003; Lodato & Rice 2005). GI occurs when the self-gravity that destabilizes the disk dominates over the restoring forces of thermal pressure and differential rotation, leading to redistribution of the disk material (e.g., Toomre 1964; Kratter & Lodato 2016). In hydrodynamical simulations, protoplanetary disks with a cooling time scale longer than the dynamical time scale settle into a quasi-stable state, as cooling balances heating from viscous dissipation (Rice et al. 2003; Cossins et al. 2009; Hall et al. 2019). In contrast, cooling with shorter time scale would result in fragmentation, which grows into one or more gravitationally bounded objects (Rice et al. 2003; Kratter & Lodato 2016). Sufficiently massive disks never really settle down, possessing fewer and more short-lived arms whose amplitude changes strongly with time (Lodato & Rice 2005). Hydrodynamical simulations based on GI can produce one, two, or more spiral arms (Laughlin & Bodenheimer 1994; Dipierro et al. 2014; Dong et al. 2015a; Hall et al. 2019), in good agreement with observations of massive protoplanetary disks (Meru et al. 2017; Tomida et al. 2017; Hall et al. 2018).

The density wave theory (Lin & Shu 1964, and references therein) predicts global-scale, GI-excited spiral density wave modes for self-gravitating unstable disks (Bertin et al. 1989). Density waves propagate through the disk and perturb the density distribution to form spiral structure (Lin & Shu 1964; Binney & Tremaine 2008; Shu 2016). Considering linear perturbations, Adams et al. (1989) derived one-armed density wave modes in protoplanetary disks, and Noh et al. (1991), Laughlin & Rozyczka (1996), and Lee et al. (2019) calculated modes with two and more arms. The behavior of density wave modes is in good agreement with numerical simulations (Laughlin & Rozyczka 1996; Laughlin et al. 1998). Theoretical studies have been carried out to analyze the mode properties, including non-linear evolution (Papaloizou & Savonije 1991), energy and angular momentum transport (Lin 2015), mode-mode interaction (Laughlin & Korchagin 1996), and mode saturation (Laughlin et al. 1997).

The degree of spiral arm winding is described by the pitch angle ( $\alpha$ ), which is defined as the angle between the tangent of the spiral and the azimuthal direction (Binney & Tremaine 2008). Large/small pitch angle corresponds to loosely/tightly wound spiral arms. It has been shown that the pitch angle of planet-excited spiral density waves becomes larger (more loosely wound) for disks with higher sound speed, disks associated with a more massive perturber (Rafikov 2002; Zhu et al. 2015),

and disks with longer cooling time scale (Zhang & Zhu 2020). In addition, the arm pitch angle increases with radius for arms interior to the perturber orbit, with the trend reversing for arms exterior to this orbit (Rafikov 2002). The arms exterior to the perturber orbit are very tightly wound (Dong et al. 2015b).

Within this backdrop, the behavior of pitch angles of GI-excited density wave modes remains somewhat unclear. Understanding such a behavior would promote our understanding of spiral arms in protoplanetary disks and may provide us a tool to distinguish the different formation mechanisms of observed spirals. In this work, we calculate two-armed spiral density wave modes in protoplanetary disks with various disk conditions, aiming to investigate the interdependence between their pitch angles and protoplanetary disk properties. We describe our analytical model and numerical solution method in Section 2. Spiral density wave modes are calculated in Section 3. The implications of our results are discussed in Section 4. Section 5 summarizes our findings.

## 2. METHOD

We numerically solve the equations of fluid dynamics to compute two-armed global spiral density wave modes in protoplanetary disks in the framework of linear density wave theory. The calculations employ a two-dimensional, razor-thin, non-viscous fluid disk, taking into consideration the kinematic effects of the central star’s gravity, disk self-gravity, and thermal pressure.

### 2.1. Linear Dynamics Equations

Adams et al. (1989) were the first to lay out the linear perturbation equations and derive one-armed density wave modes within the context of protostellar disks. We build our model based on the formalism of Adams et al. (1989), and conform to their notation system. We use cylindrical coordinates  $(r, \phi, z)$  and restrict the disk to the  $z = 0$  plane. The disk dynamics are characterized by the continuity equation (Equation 1), the radial and azimuthal momentum equations (Equation 2), Poisson’s equation (Equation 3), and the equation of state (Equation 4):

$$\frac{\partial \sigma}{\partial t} + \frac{1}{r} \frac{\partial (r \sigma u)}{\partial r} + \frac{1}{r} \frac{\partial (\sigma v)}{\partial \phi} = 0, \quad (1)$$

$$\frac{\partial u}{\partial t} + u \frac{\partial u}{\partial r} + \frac{v}{r} \frac{\partial u}{\partial \phi} - \frac{v^2}{r} = -\frac{GM_*}{r^2} - \frac{\partial (\Psi + \zeta)}{\partial r}, \quad (2a)$$

$$\frac{\partial v}{\partial t} + u \frac{\partial v}{\partial r} + \frac{v}{r} \frac{\partial v}{\partial \phi} + \frac{vu}{r} = -\frac{1}{r} \frac{\partial (\Psi + \zeta)}{\partial \phi}, \quad (2b)$$

$$\nabla^2 \Psi = 4\pi G \sigma \delta(z), \quad (3)$$

$$d\zeta = c_s^2 \frac{d\sigma}{\sigma}, \quad (4)$$

where  $u(r, \phi, t)$  denotes the radial velocity,  $v(r, \phi, t)$  the azimuthal velocity,  $M_*$  the central star mass,  $c_s$  the sound speed, following  $c_s^2 = dp/d\sigma \propto T$ ,  $\sigma(r, \phi, t)$  the surface density,  $\Psi(r, \phi, t)$  the disk self-gravity potential, and  $\zeta(r, \phi, t)$  the enthalpy. The enthalpy  $\zeta$  is used instead of the thermal pressure  $p$  for convenience of the calculation. We assume that the disk is in an adiabatic state, a widely adopted assumption in protoplanetary disk modeling (see Laughlin & Rozyczka 1996; Miranda & Rafikov 2019).

For linear analysis, we assume that the spiral perturbation is small compared with the disk background, and hence can be Fourier-analyzed in time  $t$  and azimuthal angle  $\phi$ . All the variables ( $u, v, \sigma, \Psi, \zeta$ ) can then be decomposed as

$$F(r, \phi, t) = F_0(r) + \sum_{m=1}^{\infty} F_1^m(r) e^{i(\omega_m t - m\phi)}, \quad (5)$$

where the azimuthal wavenumber  $m$  indicates the number of spiral arms. We focus on two-armed ( $m = 2$ ) spiral density wave modes, because of the prevalence of two-armed spirals among current observations: in near-infrared scattered-light observations, a significant fraction of observed spirals have two arms (e.g., Garufi et al. 2013; Benisty et al. 2015, 2017; Canovas et al. 2018; Uyama et al. 2018); millimeter continuum imaging has revealed six protoplanetary disks containing spiral structures, five of which have symmetric two-armed spirals (Andrews et al. 2018; Huang et al. 2018; Kurtovic et al. 2018). Meanwhile, massive gravitationally unstable disks, as probed in this work, tend to have low-order modes in simulations (Dong et al. 2015a; Hall et al. 2019). Higher order density waves, however, are more likely to be absorbed at the Lindblad resonance radius (see Sections 4.4 and 4.5 for further discussion).

Focusing on the  $m = 2$  mode, Equation (5) is reduced to

$$F(r, \phi, t) = F_0(r) + F_1(r) e^{i(\omega t - m\phi)}. \quad (6)$$

The equilibrium states  $F_0(r)$  of the physical properties of our protoplanetary disk models (disk mass, density profile, temperature profile, etc.) are discussed and determined in Section 3.1. We aim to numerically compute the spiral perturbation  $F_1(r)$  and the wave frequency  $\omega$ .

The real part of  $F_1(r) e^{i(\omega t - m\phi)}$  is physically meaningful. The perturbation density  $\sigma_1$  gives the density profile of the global spiral density wave modes. The wave frequency  $\omega$  is defined as  $\omega = m\Omega_p - i\gamma$ . The pattern speed  $\Omega_p$  specifies the angular velocity of the steadily rotating spiral pattern, and  $\gamma$  gives the exponential growth rate of the spiral mode. Considering quasi-steady spirals with steady morphology for at least several dynamical time scales, the mode has a constant wave frequency, i.e.,  $\Omega_p$  and  $\gamma$ , that does not vary with radius and azimuthal angle in one disk (Bertin et al. 1989).  $\Omega_p$  and  $\gamma$  are free parameters and are determined by the eigenstate of the integro-differential equation (Equation 13).

After linearization, Equations (1)–(4) become

$$i(\omega - m\Omega) \frac{\sigma_1}{\sigma_0} + \left( \frac{1}{r} + \frac{1}{\sigma_0} \frac{d\sigma_0}{dr} \right) u_1 + \frac{du_1}{dr} - \frac{im}{r} v_1 = 0, \quad (7)$$

$$i(\omega - m\Omega) u_1 - 2\Omega v_1 = -\frac{d(\Psi_1 + \zeta_1)}{dr}, \quad (8a)$$

$$i(\omega - m\Omega) v_1 + \frac{\kappa^2}{2\Omega} u_1 = \frac{im}{r} (\Psi_1 + \zeta_1), \quad (8b)$$

$$\Psi_1(r) = -\int_{R_{\text{inn}}}^{R_{\text{out}}} d\rho \int_0^{2\pi} \frac{G \cos(m\phi) \sigma_1(\rho) \rho}{\sqrt{\rho^2 + r^2 - 2\rho r \cos \phi}} d\phi, \quad (9)$$

$$\zeta_1 = c_s^2 \frac{\sigma_1}{\sigma_0}, \quad (10)$$

where subscript 0 denotes the equilibrium state and subscript 1 denotes spiral perturbation quantities. The angular velocity of the equilibrium state is

$$\Omega = \sqrt{\frac{1}{r} \left( \frac{GM_*}{r^2} + \frac{d\Psi_0}{dr} + \frac{d\zeta_0}{dr} \right)}, \quad (11)$$

with epicyclic frequency

$$\kappa^2 = \frac{1}{r^3} \frac{d}{dr} [(r^2 \Omega)^2]. \quad (12)$$

Combining Equations (7)–(10), we eliminate other variables and get a second-order integro-differential equation of the perturbation density  $\sigma_1(r)$  and wave frequency  $\omega$ :

$$\left[ \frac{d^2}{dr^2} + A(\omega, r) \frac{d}{dr} + B(\omega, r) \right] (\zeta_1 + \Psi_1) + C(\omega, r) \zeta_1 = 0, \quad (13)$$

where the coefficients  $A$ ,  $B$ , and  $C$  are given by

$$A = \frac{d}{dr} \ln \left[ \frac{\sigma_0 r}{\kappa^2 (1 - \nu^2)} \right], \quad (14)$$

$$B = -\frac{m^2}{r^2} - \frac{4m\Omega}{\kappa(1-\nu^2)r} \frac{d\nu}{dr} + \frac{2m\Omega}{\kappa\nu r} \frac{d}{dr} \ln\left(\frac{\kappa^2}{\Omega\sigma_0}\right), \quad (15)$$

$$C = -\frac{\kappa^2(1-\nu^2)}{c_s^2}. \quad (16)$$

In these equations, the Doppler-shifted frequency is defined as

$$\nu = \frac{\omega - m\Omega}{\kappa}. \quad (17)$$

Together with the boundary conditions defined in Section 2.2, Equation (13) becomes a well-defined integro-differential equation. We then numerically solve Equation (13) without further approximation and obtain  $\sigma_1(r)$  and  $\omega$  (Section 2.3).

### 2.2. Boundary Condition

Following the strategy of Noh et al. (1991), we adopt two different inner boundary conditions: reflecting (R) and transmitting (T). For a reflecting boundary condition, the radial velocity is set to vanish ( $u_1 = 0$ ), resulting in

$$\left(\frac{d}{dr} - \frac{2m\Omega}{\omega - m\Omega} \frac{1}{r}\right) (\Psi_1 + \zeta_1) = 0. \quad (18)$$

For a transmitting boundary condition, we assume that the trailing waves propagate through disk boundaries, which requires

$$d\sigma_1/dr + i|k|\sigma_1 = 0, \quad (19)$$

with the wave number  $|k|$  obtained from the dispersion relation (see Equation 24)

$$|k| = \frac{\pi G\sigma_0}{c_s^2} + \frac{\pi G\sigma_0}{c_s^2} \{1 - Q^2 [1 - (\omega - m\Omega)^2/\kappa^2]\}^{1/2}. \quad (20)$$

We adopt three different outer boundary conditions: confining pressure boundary condition (C), as well as the reflecting and transmitting boundary conditions. Confining pressure is set where the disk is conjuncted with the outer environment, leading to a constant background pressure. Requiring that the Lagrangian pressure perturbation  $\Delta p = 0$ , and hence  $\Delta\sigma = 0$ ,

$$\sigma_1 = \frac{1}{\kappa^2 - (\omega - m\Omega)^2} \frac{d\sigma_0}{dr} \left(\frac{d}{dr} - \frac{2m\Omega}{\omega - m\Omega} \frac{1}{r}\right) (\Psi_1 + \zeta_1). \quad (21)$$

As discussed in Section 4.2, the boundary conditions influence the wave behavior near the boundaries and the wave feedback process.

### 2.3. Numerical Method

We solve the integro-differential Equation (13) using the matrix-eigenvalue method described in Adams et al. (1989). We briefly summarize the key steps and leave additional details to Appendix A. In this method, Equation (13) eventually turns into an eigenvalue problem, with  $\omega$  and  $\sigma_1$  being the eigenfrequency and eigenfunction. This eigenvalue method has been widely adopted in searching for global normal modes in planetary rings, galaxy disks, and protostellar disks (e.g., Papaloizou & Lin 1989; Noh et al. 1991; Laughlin & Rozyczka 1996; Feng et al. 2014; Lee et al. 2019).

We set  $N = 500$  logarithmically spaced radial grid points to discretize Equation (13), aiming to solve the value of  $\sigma_1(r)$  at each grid point and  $\omega$  for each eigenmode. For convenience, our calculation uses dimensionless  $S(r) = \sigma_1(r)/\sigma_0(r)$  instead of  $\sigma_1(r)$ .  $S(r)$  is then replaced by the  $N$ -dimensional vector  $\mathbf{S}$ , which contains  $N$  values of  $S(r)$  at each grid point. Likewise, all the functions and operators in Equation (13) are replaced by  $N \times N$  matrices (Appendix A), turning it into the matrix equation

$$\mathcal{W}(\omega)\mathbf{S} = 0. \quad (22)$$

The  $N \times N$  matrix  $\mathcal{W}(\omega)$  is a fifth-order function of  $\omega$ . We analytically regroup Equation (22) into the  $5N$ -dimensional

$$\mathcal{T}\mathbf{S}_d = \omega\mathcal{Z}\mathbf{S}_d, \quad (23)$$

which is a standard eigenvalue problem, where  $\mathbf{S}_d$  is analytically equivalent to  $\mathbf{S}$ . We refer the reader to Appendix A for the detailed transformation process. Solving the eigenfunction and eigenfrequency of Equation (23) gives the perturbation density  $\mathbf{S}$  and wave frequency  $\omega$ . Equation (23) has  $5N$  eigenmodes, only a few of which have non-zero growth rate. We choose the eigenmode with the highest growth rate as our final spiral density wave mode, as it would grow exponentially faster and dominate over the other modes (Adams et al. 1989; Bertin et al. 1989). We note that linear analysis is unable to give the amplitude of  $\sigma_1$ , as  $\sigma_1$  can be multiplied by an arbitrary factor, as seen in Equation (13). Information on the amplitude is lost when  $F_1 \ll F_0$  is assumed. In our numerical calculation, we employ a unit system in which the outer disk radius  $R_d$ , the central star mass  $M_*$ , the gravitational constant  $G$ , and the Keplerian angular velocity at the disk outer boundary ( $\Omega_K = G^{1/2}M_*^{1/2} \cdot R_d^{-3/2}$ ) are set to unity. The angular velocity, pattern speed, and growth rate in our calculation have the units of  $\Omega_K$ .

The two-dimensional gravitational potential calculation has a singularity that needs special care. To deal with the singularity, we soften the gravity by adding a term  $\eta^2 r^2$  with  $\eta \ll 1$  (Laughlin et al. 1997; Tremaine 2001) to the denominator of Equation (9) (for details, see Appendix A).

### 3. RESULTS

We numerically calculate two-armed spiral density wave modes in protoplanetary disks of various physical properties. We use pitch angle to characterize the degree of arm winding, and then study the interdependence between spiral pitch angles and disk properties.

#### 3.1. Disk Properties

To probe the spiral density wave modes generated by GI, we consider massive protoplanetary disks with disk-to-star mass ratio ranging from  $M_d/M_* \approx 0.1$  to 0.5. These disks are sufficiently massive that the disk self-gravity plays an important role. It has been shown, based on both theory and simulations, that GI in protoplanetary disks occurs when  $M_d/M_* \gtrsim 0.1$  (Adams et al. 1989; Noh et al. 1991; Dong et al. 2015a; Hall et al. 2018). In contrast, observations give typical disk masses of  $M_d/M_* \approx 0.01$  (Andrews et al. 2013; Dong et al. 2018b). Disk masses derived from current observations, however, have large uncertainties and may be underestimated (Kratter & Lodato 2016; Dong et al. 2018a). In addition, massive disks may exist in an earlier evolutionary stage (Kratter & Lodato 2016). Section 4.4 presents further discussion.

GI is quantified by Toomre’s (1964) parameter  $Q = \kappa c_s / \pi G \sigma_0$ . A smaller  $Q$  generally indicates a more unstable disk. The condition that  $Q \lesssim 1$  is the threshold of axisymmetric instability, while the threshold value of  $Q$  is greater than unity for non-axisymmetric spiral perturbations (Kratter & Lodato 2016). We utilize the mass-weighted average value of  $\bar{Q} = \int Q \sigma_0 dS / \int \sigma_0 dS$ , where  $S$  denotes the surface area, to characterize the disk stability, and focus on marginally stable disks with  $1 \lesssim \bar{Q} \lesssim 2$ . In this case, the disks are stable to axisymmetric perturbation but unstable to non-axisymmetric spiral perturbation, as shown in our resulting density wave modes.

We make use of two kinds of surface density profiles: power law disk and Gaussian disk. The power law density profile follows  $\sigma_0(r) = \Sigma r^{-p}$ , which is widely adopted in both observational (Wilner et al. 2000; Piétu et al. 2006; Andrews et al. 2009; Grady et al. 2013) and theoretical (Papaloizou 2002; Dong et al. 2015a; Hall et al. 2018) studies. The value of  $p$  ranges from 0 to 2. The Gaussian profile,  $\sigma_0(r) = \Sigma e^{-(r-R_0)^2/w}$ , characterizes more evolved disks with inner disk region beginning

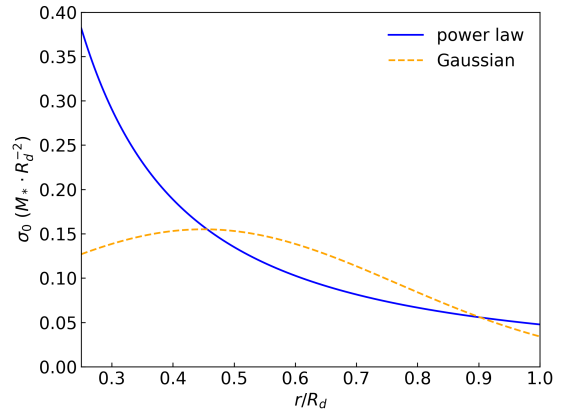


**Figure 1.** Surface density profiles of the fiducial power law disk ( $\sigma_0 = \Sigma^p r^{-1.5}$ ; blue solid line) and the fiducial Gaussian disk ( $\sigma_0 = \Sigma^G e^{-(r-0.45)^2/0.2}$ ; orange dashed line) with  $M_d/M_* = 0.3$ .

to be depleted (e.g., Laughlin et al. 1997; Boehler et al. 2017; Pinilla et al. 2018). We adopt  $p = 1.5$ ,  $R_0 = 0.45$ , and  $w = 0.2$  in our models. The normalization factor  $\Sigma$  is determined by the disk mass. Figure 1 illustrates the density profiles of the fiducial disk for each kind.

We utilize a power law temperature profile  $T_0(r) = T_k r^{-q}$ , which is widely used in fitting observations (Andrews et al. 2011; Muto et al. 2012; Dullemond et al. 2020),  $q \approx 0.1 - 1$ . For a disk in which cooling by self-radiation balances heating from irradiation of the central star, the temperature profile, depending on disk flaring, has a varying  $q$ , which typically equals  $3/7$  (Chiang & Goldreich 1997; Kratter & Lodato 2016). If cooling balances heating by the release of gravitational potential energy via accretion, the temperature profile has  $q = 3/4$  (Kratter & Lodato 2016). Our models adopt an intermediate value of  $q = 0.6$ . The aspect ratio  $h = c_s / (\Omega r)$  characterizes the disk thickness. As  $\Omega \propto r^{-1.5}$ , we have  $h \propto r^{0.2}$  in our models, indicating a nearly constant flare angle. The mass-weighted average aspect ratio is defined as  $\bar{h} = \int h \sigma_0 dS / \int \sigma_0 dS$ . The normalized factor  $T_k$  in the temperature profile is determined by  $\bar{Q}$  or  $\bar{h}$  through the sound speed  $c_s$ .

The radial extent of our disk models is set from 25 AU to 100 AU. The region near the central star is excluded, considering that central disk region can be depleted and involve non-linear processes (Andrews et al. 2011). The influence of boundary conditions on the resulting density wave modes was tested (discussed in Section 4.2). Spiral wave modes in disks with different boundaries generally show similar morphology and pitch angle. In our following calculations, we use two representative groups of boundary conditions: (1) reflecting inner boundary and transmitting outer boundary for power law disk, and (2)

reflecting inner boundary and confining pressure outer boundary for Gaussian disk. Current observations provide little constraint on the physical properties of the disk boundaries. We choose these two groups in order to consider both reflecting and transmitting density waves in the disks.

### 3.2. Fiducial Disks

We use the power law disk and the Gaussian disk with  $M_d/M_* = 0.3$  and  $\bar{Q} = 1.40$  as the two fiducial disks of our calculations, which have disk mass and Toomre  $Q$  values in the middle of our survey range (Section 3.1). The resulting two-armed spiral mode of the fiducial power law disk is illustrated in Figure 2. The left panel presents the two-dimensional distribution of spiral density wave ( $\text{Re}[\sigma_1(r)e^{-im\phi}]$ ) on a logarithmic scale, and the right panel shows the amplitude of the perturbation density as a function of radius ( $|\sigma_1(r)|$ ). This mode has pattern speed  $\Omega_p = 2.61$  and growth rate  $\gamma = 0.243$  (in units of  $\Omega_K$ , the Keplerian velocity at the disk outer boundary). Figure 3 presents the results for the fiducial Gaussian disk, with  $\Omega_p = 1.57$  and  $\gamma = 0.242$ . The corotation radius [CR;  $\Omega(r = \text{CR}) = \Omega_p$ ] marks the radius in which the rotational speed is equal to the pattern speed of spiral arms, and the CR lies between the inner Lindblad radius and the outer Lindblad radius, as marked in Figures 2 and 3. In both of the two fiducial disks, the two-dimensional distribution of spiral density wave clearly shows two symmetric, trailing spiral arms, which extend over  $270^\circ$  in the azimuthal direction. The quantity  $|\sigma_1(r)|$  is the relative amplitude of the perturbation density, normalized by the maximum value, along the ridges of the spiral arms. The amplitude  $|\sigma_1(r)|$  fluctuates with radius, as can be seen in both the radial profile and two-dimensional density distribution.

The principal range for the propagation of spiral density waves lies between the inner Lindblad radius (ILR;  $\Omega_p = \Omega - \kappa/m$ ) and the outer Lindblad radius (OLR;  $\Omega_p = \Omega + \kappa/m$ ) (Bertin & Lin 1996). The density waves are absorbed at the Lindblad resonances (Lynden-Bell & Kalnajs 1972; Goldreich & Tremaine 1978, 1979). Therefore, for our study of global spiral density wave modes, we restrict the permitted region for the density waves to the region between the ILR and OLR. As seen in Figures 2 and 3, our calculated density wave modes generally have continuous spiral arms with smooth morphology between the two resonances. In contrast, structures outside the ILR and OLR have abnormal appearances. In the fiducial power law disk (Figure 2), a lump piles up between the OLR and the outer boundary, likely due to the imposed outer boundary condition. In the fiducial Gaussian disk (Figure 3), structures inside the

ILR resemble a set of alternating bananas (also seen in Adams et al. 1989). This structure may arise from the interference of trailing and leading waves with comparable amplitudes. In the principal region where the growth rate of the spiral mode is comparable to the rotation period, the trailing wave dominates over the leading wave and forms continuous spiral arms.

### 3.3. Measurement of Spiral Pitch Angle

The pitch angle describes the degree of spiral arm winding. Smaller pitch angles correspond to more tightly wound spiral arms, and vice versa. To measure the pitch angles of our spiral density wave modes, we trace the points of maximum perturbation density (the ridge) at each radius. Fitting the points with a logarithmic function,  $\phi = \beta \ln r + \phi_0$ , the pitch angle  $\alpha = \arctan(1/\beta)$ . We only consider the spiral density waves in the permitted region from the ILR to the OLR, to mitigate possible adverse effects of the imposed boundary conditions. The best-fit function is illustrated as white curves in Figures 2 and 3. Our fiducial power law disk has pitch angle  $\alpha = 13^\circ 07'$ , and the fiducial Gaussian disk has  $\alpha = 9^\circ 61'$ . Although we restrict to this particular radial range, fitting over the entire disk does not adversely affect our results significantly, yielding  $\alpha = 12^\circ 13'$  for the fiducial power law disk and  $\alpha = 9^\circ 18'$  for the fiducial Gaussian disk.

### 3.4. Interdependence Between Spiral Pitch Angle and Disk Properties

In order to understand the behavior of spiral pitch angles, we perform a survey study of two-armed spiral density wave modes on various disk conditions. In our survey, we consider the effect of three parameters: disk-to-star mass ratio ( $M_d/M_*$ ), average Toomre  $Q$  ( $\bar{Q}$ ), and average aspect ratio ( $\bar{h}$ ). The surface density profile, temperature profile, and boundary conditions remain the same as for the fiducial disks. The three parameters are connected with each other (see Section 3.1). We thus have one parameter fixed and one vary, and then observe the variations of spiral pitch angle. We calculate the density wave modes in both power law disks and Gaussian disks.

Figure 4 displays four wave modes in power law disks with  $\bar{Q}$  increasing from 1 to 1.9 for a given  $M_d/M_* = 0.3$ . Clear symmetric spiral patterns are present, which become progressively more loosely wound as  $\bar{Q}$  rises. More loosely wound spiral arms cover smaller azimuthal extension, while tightly wound spirals can wind up more than one round. Figure 4 illustrates examples in Gaussian disks with  $M_d/M_*$  increasing from 0.2 to 0.5 for a given  $\bar{h} = 0.12$ . The resulting spiral patterns become

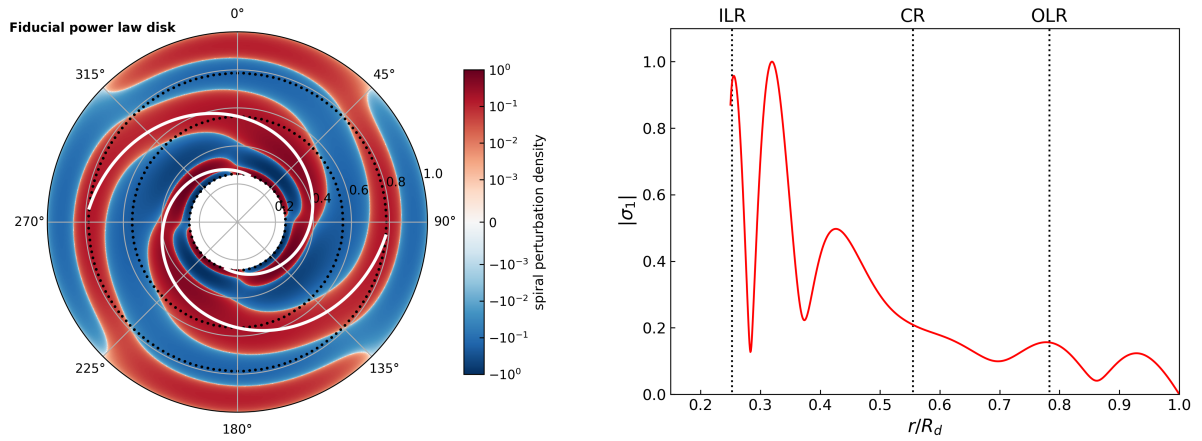


**Figure 2.** Illustration of our calculated spiral density wave mode in the fiducial power law disk. (Left) Two-dimensional distribution of spiral perturbation density on a logarithmic scale, with white curves denoting fitted peak arm position, and inner, middle, and outer dotted circles marking the inner Lindblad (ILR), corotation (CR), and outer Lindblad (OLR) radius, respectively. The spiral pattern between the two Lindblad radii is physically meaningful. (Right) Radial profile of normalized perturbation density  $|\sigma_1(r)|$ , reflecting the amplitude along the spiral arms in the left panel.

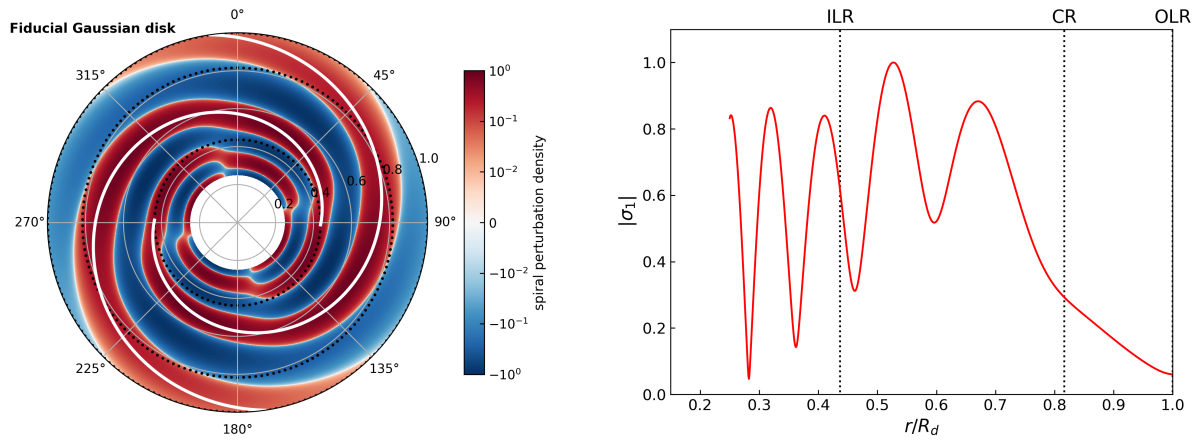


**Figure 3.** Illustration of our calculated spiral density wave mode in the fiducial Gaussian disk, presented in the same way as in Figure 2.

### Power law disks

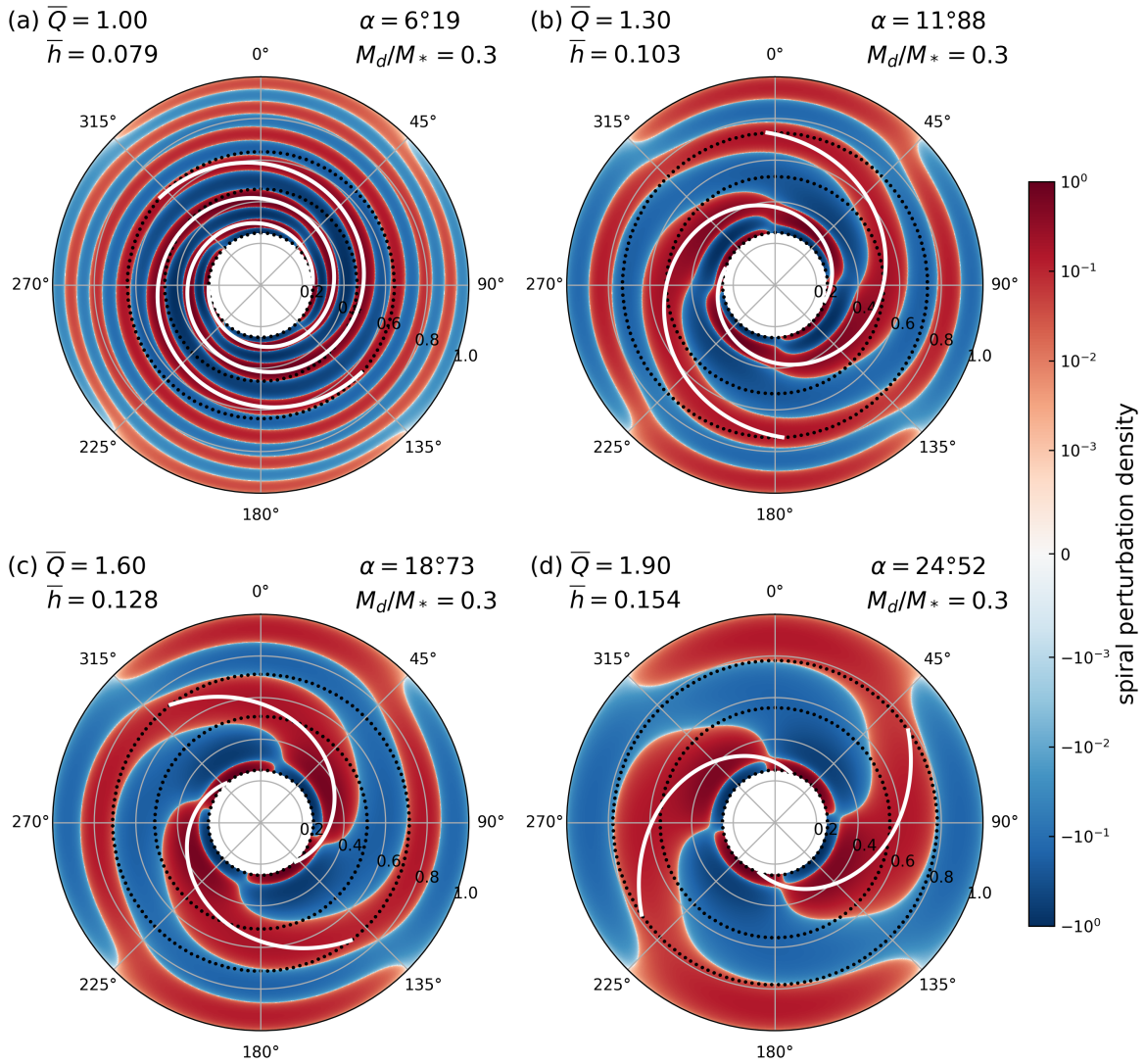


**Figure 4.** Morphology of spiral density wave modes in power law disks with fixed  $M_d/M_* = 0.3$  and (a)  $\bar{Q} = 1.00$ ,  $\alpha = 6^\circ:19$ ; (b)  $\bar{Q} = 1.30$ ,  $\alpha = 11^\circ:88$ ; (c)  $\bar{Q} = 1.60$ ,  $\alpha = 18^\circ:73$ ; and (d)  $\bar{Q} = 1.90$ ,  $\alpha = 24^\circ:52$ . The value of  $\bar{h}$  changes accordingly, as  $\bar{h}$  connects with  $\bar{Q}$ .

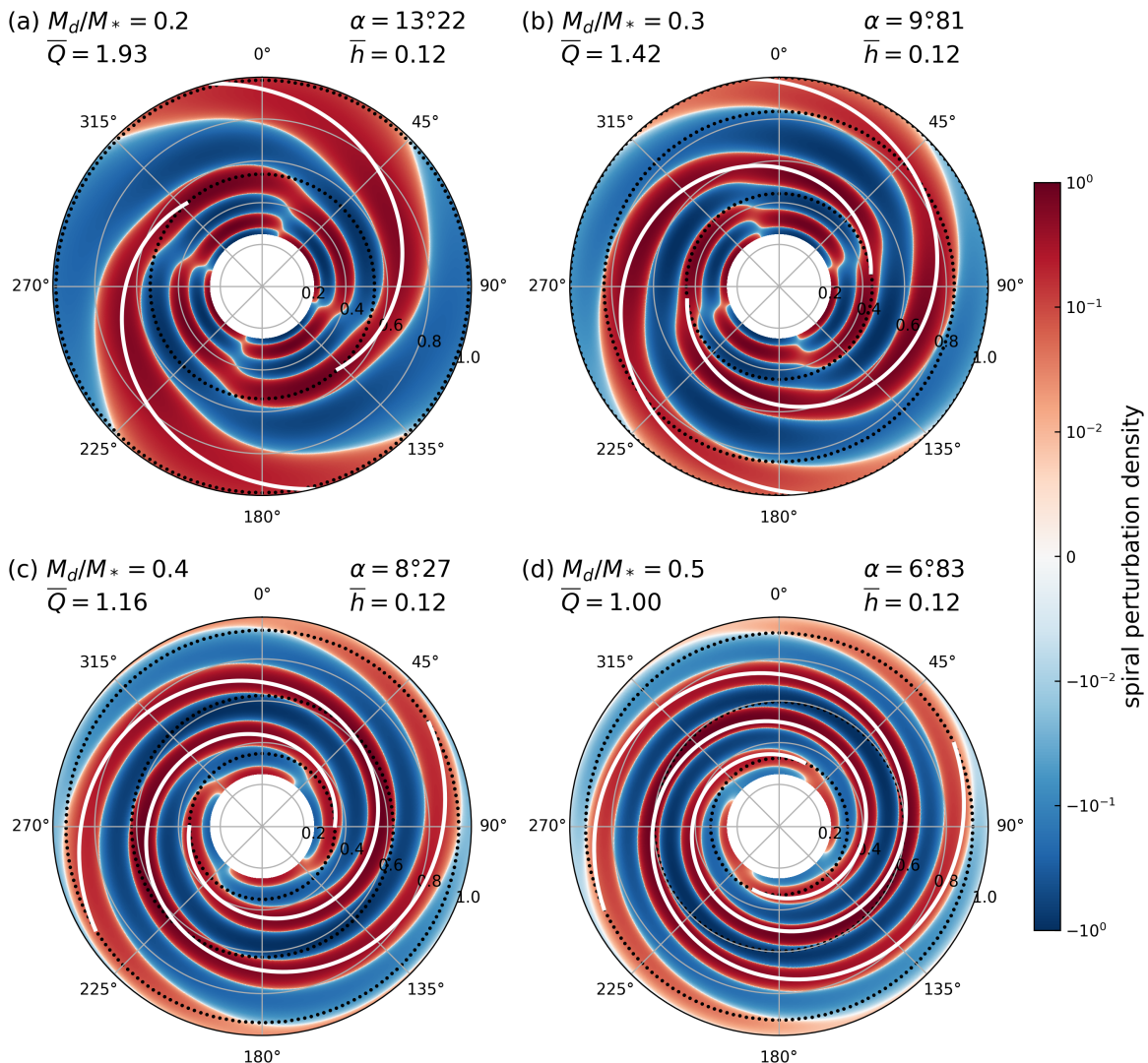
more tightly wound as  $M_d/M_*$  increases. Compared with power law disks, the spirals of Gaussian disks have a larger OLR, which is close to the outer boundary of the disk.

Figure 6 presents the interdependence between spiral pitch angles of our density wave modes, measured as in Section 3.3, and the three main parameters of protoplanetary disks. The blue points and orange squares mark, respectively, the results of power law and Gaussian disks. The pitch angles in our survey, which range from  $\alpha \approx 5^\circ$  to  $30^\circ$ , exhibit the following trends:

- For a fixed  $\bar{Q}$ , a heavier disk (hence larger aspect ratio) has spirals with larger pitch angle (Figure 6a).
- For a fixed  $\bar{h}$ , a heavier disk is more unstable (smaller  $\bar{Q}$ ) and has spirals with smaller pitch angle (Figure 6b).
- For a fixed  $M_d/M_*$ , disks with higher  $\bar{Q}$  or higher  $\bar{h}$  show spirals with larger pitch angles (Figures 6c and 6d).
- Under the same conditions, spirals in a Gaussian disk have smaller pitch angles than those in a power law disk.



### Gaussian disks



**Figure 5.** Morphology of spiral density wave modes in Gaussian disks with fixed  $\bar{h} = 0.12$  and (a)  $M_d/M_* = 0.2$ ,  $\alpha = 13:22$ ; (b)  $M_d/M_* = 0.3$ ,  $\alpha = 9:81$ ; (c)  $M_d/M_* = 0.4$ ,  $\alpha = 8:27$ ; and (d)  $M_d/M_* = 0.5$ ,  $\alpha = 6:83$ .

## 4. DISCUSSION

### 4.1. Analytical Approach and Implications for the Relationship between Pitch Angle and Disk Properties

Our numerical calculations give the relationships between spiral pitch angle and disk properties. To understand the physics behind these trends, we follow [Lin & Shu \(1964\)](#) and employ a widely used dispersion relation of density wave theory to connect the radial wave number with disk properties:

$$(\omega - m\Omega)^2 = k^2 c_s^2 - 2\pi G\sigma_0 |k| + \kappa^2. \quad (24)$$

The dispersion relation, derived through the Wentzel-Kramers-Brillouin (WKB) approximation, requires that

the phase of the perturbation changes rapidly with radius ( $|kr| \gg 1$ ), such that long-range gravitational coupling is negligible and the wave behavior is determined by local dynamics. Given these assumptions, the dispersion relation works most effectively for tightly wound spiral arms, but still applies to more open and global spirals ([Binney & Tremaine 2008](#); [Shu 2016](#)).

The spiral pitch angle  $\alpha \approx \partial r / (r \partial \phi) \approx m / (|k|r)$  ([Binney & Tremaine 2008](#)). The right-hand side quantity of Equation (24) has a minimum value at  $|k| = \pi G\sigma_0 / c_s^2$ , for which the corresponding  $\omega$  has the largest growth

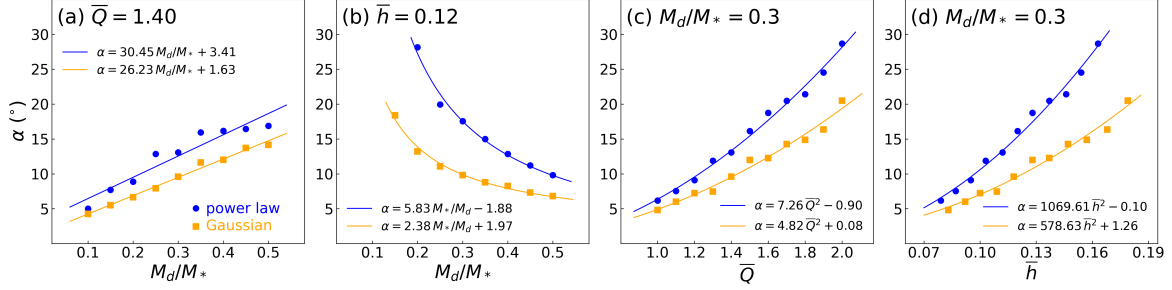


**Figure 6.** The dependence of the pitch angle ( $\alpha$ ) of spiral density waves in power law disks (blue dots) and Gaussian disks (orange squares) with (a) disk-to-star mass ratio ( $M_d/M_*$ ), with average Toomre  $Q$  fixed to  $\bar{Q} = 1.40$ , (b)  $M_d/M_*$ , with average aspect ratio fixed to  $\bar{h} = 0.12$ , (c)  $\bar{Q}$ , with  $M_d/M_* = 0.3$ , and (d)  $\bar{h}$ , with  $M_d/M_* = 0.3$ . The fitted functions of  $\alpha$  and the various parameters are shown as blue (power law) and orange (Gaussian) curves in each panel.

rate (Cossins et al. 2009). For this most unstable mode, the pitch angle

$$\alpha \approx \frac{mc_s^2}{\pi G \sigma_0 r}. \quad (25)$$

Averaging along radius, the pitch angle estimated by Equation (25) gives  $\alpha = 15^\circ 44$  for the fiducial power law and  $13^\circ 80$  for the fiducial Gaussian disk, while our numerical calculation gives  $\alpha = 13^\circ 07$  and  $9^\circ 61$ , respectively. In our disk models, the pitch angle in Equation (25) is nearly constant along the radius; for instance, for the power law disk,  $\alpha \propto r^{-0.1}$ . Because of the weak dependence on radius and the similar disk size in our models, we drop the variable  $r$  from the discussions below, and Equation (25) becomes

$$\alpha \propto \frac{c_s^2}{\sigma_0}. \quad (26)$$

A denser disk with lower sound speed has more tightly wound spiral arms. If we replace  $c_s$  and  $\sigma_0$  by  $M_d/M_*$ ,  $Q$ , or  $h$ , and consider Keplerian  $\Omega$  and  $\kappa$ , Equation (26) yields the following trends:

1. When  $Q$  ( $\propto \sqrt{M_*} c_s / M_d$ ) is fixed, increasing  $M_d/M_*$  elevates  $c_s$ . Because of the quadratic dependence of  $c_s$  in Equation (26), pitch angle accordingly increases. This results in the trend  $\alpha \propto \bar{Q}^2 M_d/M_* \propto M_d/M_*$  (Figure 6a).
2. When  $h$  ( $\propto c_s / \sqrt{M_*}$ ) is fixed,  $c_s$  remains unchanged. Pitch angle decreases as  $M_d/M_*$  increases. This results in the trend  $\alpha \propto \bar{h}^2 M_*/M_d \propto (M_d/M_*)^{-1}$  (Figure 6b).
3. When  $M_d/M_*$  is fixed, increasing of  $Q$  or  $h$  leads to higher  $c_s$ , and hence larger pitch angle. This results in the trend  $\alpha \propto \bar{Q}^2 M_d/M_* \propto \bar{Q}^2$  (Figure 6c) and  $\alpha \propto \bar{h}^2 M_*/M_d \propto \bar{h}^2$  (Figure 6d).

We further fit the resulting dependence of pitch angle on  $M_d/M_*$ ,  $M_*/M_d$ ,  $\bar{Q}^2$ , and  $\bar{h}^2$  (Figure 6). These new relations, especially that between  $\alpha$  and  $M_*/M_d$ , can successfully fit our numerical results, suggesting that the trends involving the pitch angle of our spiral density wave modes can be explained uniformly by Equation (26), in spite that Equation (26) involves WKB approximation. Therefore, the reason why Gaussian disks have smaller pitch angles than power law disks is that, between the two Lindblad resonances, for the same total mass there is a broader radial extent in which the surface density of a Gaussian disk is higher than that of a power law disk (Figure 1). This suggests that more evolved disks should have more tightly wound spirals, as the surface density profiles of evolved disks tend to be close to Gaussian (Laughlin et al. 1997; Boehler et al. 2017; Pinilla et al. 2018).

Consistent with the trend of our density wave modes (Figure 6a), the GI-excited spiral arms generated in hydrodynamical simulations of marginally stable ( $Q \approx 1$ ) disks tend to be more open (larger pitch angle) in more massive disks (Cossins et al. 2009). Evidence supporting the dependence on disk mass and sound speed (Equation 26) has been found in observational studies. Yu et al. (2019), studying the spiral pitch angles of 13 protoplanetary disks with a narrow range of disk aspect ratio (0.06 – 0.12), found that more massive disks, that are hence more unstable, have smaller pitch angles, consistent with the trend in Figure 6b. However, the low-mass end of their correlation is less likely to be explained by GI-excited wave modes, as the corresponding disks are too stable. Near-infrared scattered-light imaging observes the structure on the disk surface, while millimeter continuum imaging detects the cold dust in the disk midplane. The spiral arms of MWC 758 imaged in near-infrared scattered light are more open than their counterparts observed in the millimeter continuum, which may be due in part to the higher sound speed on the disk surface, but the main cause is the combined geomet-

**Table 1.** Influence of Boundary Conditions

Boundary	$\Omega_p^P$	$\gamma^P$	$\alpha^P$	$\Omega_p^G$	$\gamma^G$	$\alpha^G$
Conditions	( $\Omega_K$ )	( $\Omega_K$ )	( $^\circ$ )	( $\Omega_K$ )	( $\Omega_K$ )	( $^\circ$ )
RR	2.56	0.136	12.92	1.11	0.468	8.85
RT	2.61	0.243	13.07	1.35	0.374	9.34
RC	2.61	0.240	13.09	1.57	0.242	9.61
TR	2.32	0.193	14.30	1.11	0.483	8.76
TT	2.30	0.241	14.08	1.39	0.386	9.40
TC	2.30	0.242	14.10	1.18	0.328	8.88

NOTE—Parameters of spiral density wave modes of our fiducial power law (noted with p) and Gaussian (noted with G) disk calculated by adopting different boundary conditions. The first and second letters of the abbreviation in the first column denote the inner and outer boundary conditions: R = reflecting, T = transmitting, and C = confining pressure. The Keplerian rotation speed at the disk outer boundary is  $\Omega_K$ .

ric effect of a cone-shaped surface and a flat midplane (Dong et al. 2018a). There is a degree of similarity between the GI-excited spiral density waves studied in this work and planet-excited density wakes. Similar to our results, planet-excited arms are more open in disks with higher sound speed (Rafikov 2002), in spite of the additional dependence on radius and planet mass (Rafikov 2002; Zhu et al. 2015). The pitch angle of planet-excited spirals has similar but weaker dependence on disk mass, if  $Q$  is close to unity (Zhang & Zhu 2020). Inefficient cooling, by raising the sound speed (Zhang & Zhu 2020), is also expected to impact the pitch angle of our density wave modes in the same manner. We note that, unlike planet-excited spirals, disks with high  $Q$  ( $\gtrsim 2$ ) are unable to generate GI-excited spiral density waves because of the inadequate growth rate.

#### 4.2. Influence of Boundary Conditions

We investigate the influence of boundary conditions on the density wave modes by altering the boundary conditions adopted in our fiducial disks (see Section 2.2). The parameters of the resulting wave modes are listed in Table 1. All the wave modes have considerable growth rate and thus exist. The typical fractional change of pitch angle or pattern speed induced by the adoption of different boundary conditions is about 10%. We conclude that our wave modes are not an artificial result of certain boundary conditions and that the usage of boundary conditions will not significantly influence the derived pitch angle or pattern speed.

Boundary conditions affect the growth rate (e.g., Noh et al. 1991). As Table 1 illustrates, the growth rates of wave modes with reflecting (R), transmitting (T), and confining pressure (C) inner/outer boundaries generally show the tendency for  $\gamma_R < \gamma_T \approx \gamma_C$  for the fiducial power law disk. By comparison, with the exception of  $\gamma_R < \gamma_T$  for inner boundary,  $\gamma_R > \gamma_T > \gamma_C$  for the fiducial Gaussian disk. One possible reason is that the reflected wave at the boundary constructively/destructively interferes, resulting in larger/smaller growth rate than those with a transmitting boundary (Shu 2016). Another possibility is that, owing to the WKB approximation, our transmitting boundary is not exactly accurate and some reflection may affect the growth rate (Noh et al. 1991). The real boundaries of protoplanetary disks can be combinations of these three idealized boundaries, or perhaps even more complicated.

#### 4.3. Radial Variation of Spiral Amplitude and Pitch Angle

In our spiral density wave modes, the amplitude of the arms fluctuates with radius, as can be seen in the dips and bumps in Figures 2 and 3. GI-excited spirals in numerical simulations exhibit a saturation amplitude with less fluctuation (Cossins et al. 2009). In contrast, the amplitude of planet-launched spirals piles up to a maximum that depends on the planet mass, followed by a decline toward the planet (Zhu et al. 2015). Recent ALMA observations of spiral arms in protoplanetary disks reveal profiles of fluctuating amplitudes (Huang et al. 2018) that resemble those seen in our spiral mode analysis. In particular, the spiral amplitude profiles of Elias 27, WaOph 6, and IM Lup have, respectively, one, two, and three main bumps. Confirming whether they correspond to the density wave modes studied in this work requires detailed modeling, and will be addressed in future work.

The spiral pitch angle of our calculated density wave modes also varies with radius. We trace the spiral arms by the points of maximum perturbation density at each radius, and we use the slope of their azimuthal angle  $\phi(r)$  to indicate the pitch angle, as  $\alpha(r) \approx \partial r / (r \partial \phi)$ . We estimate  $\alpha(r)$  by fitting a logarithmic function (Section 3.3) to the  $(\phi, r)$  diagram at each radius, using a window of 30 points centered on that radius. For the same disk properties, Gaussian disks present a similar radial variation of pitch angle as power law disks (not shown), but with larger extension of continuous spiral arms. We thus focus on the results of  $\phi(r)$  and  $\alpha(r)$  based on Gaussian disks (Figure 7); the purple solid, red dashed, green dashed-dotted, and blue dotted curves

mark the result for the disk with  $(M_d/M_*, \bar{Q}) = (0.5, 1.00)$ ,  $(0.5, 1.40)$ ,  $(0.3, 1.40)$ , and  $(0.3, 1.80)$ , respectively. The radial variation of pitch angle of our density wave modes is related to the disk mass and sound speed. Massive cool disks have pitch angle falling with radius, while low-mass hot disks have pitch angle rising with radius, although oscillations exist in these radial profiles. Interestingly, the pitch angle of GI-excited spiral arms generated in numerical simulations exhibit little radial variation (e.g., Cossins et al. 2009; Forgan et al. 2018).

By contrast, the pitch angle of planet-excited spiral wakes increases with radius toward the position of the perturber, beyond which the trend reverses (Rafikov 2002; Zhu et al. 2015). We suggest that the radial variation of spiral amplitude and pitch angle potentially provides an effective diagnostic tool to distinguish between planet-excited wakes and GI-excited global density waves.

#### 4.4. Excitation and Propagation of the Density Wave Mode

Disk mass is a crucial parameter for GI to occur. Spiral arms observed in protoplanetary disks with low mass ( $\sim 0.01M_*$ ) are less likely to be excited by GI, and, instead, are probably driven by an embedded planet (Dong et al. 2015b, 2016b; Fung & Dong 2015; Zhu et al. 2015). GI-excited spiral arms prefer early-type (Class 0, Class I, and the earliest Class II) protoplanetary disks, which are more massive and fed by infall from their surrounding envelope (e.g., Dong et al. 2016a; Pérez et al. 2016; Meru et al. 2017; Tomida et al. 2017). Nevertheless, it is worth noting that the disk mass, based on the dust mass derived from observations of the millimeter and submillimeter continuum emission, has large uncertainty. The disk mass can be underestimated if the dust is optically thick, grain growth has occurred, or the gas-to-dust mass ratio is larger than assumed (Pérez et al. 2012; Kratter & Lodato 2016). On the other hand, the high stellar accretion rate of Herbig stars indicates that disk masses could be much larger than those inferred from dust emission (Dong et al. 2018b). More accurate measurement of disk masses in the future can help determine whether GI plays an important role in protoplanetary disks.

A density wave gets absorbed in the Lindblad resonances and thus mainly exists between the ILR and OLR (Adams et al. 1989; Bertin & Lin 1996). The density wave will not remain in a fixed position, but propagates radially as a wave packet with a group velocity given by

$v_g = \partial\omega(k, r)/\partial k$  (Toomre 1969). We make use of the dispersion relation (Equation 24) to estimate

$$v_g(r) = \pm \frac{|k|c_s^2 - \pi G\sigma_0}{\omega - m\Omega}. \quad (27)$$

Figure 8 plots  $v_g(r)$ , in units of the Keplerian linear velocity at the disk outer boundary, for the spiral density wave modes of the two fiducial disks. The average group velocity over the region between the ILR and OLR is  $\bar{v}_g = 0.127$  for the power law disk and  $\bar{v}_g = 0.137$  for the Gaussian disk. The time scale for the density wave to travel from the ILR to the OLR is thus  $t \approx \Delta R/\bar{v}_g \approx 0.7\tau$ , where  $\tau$  is the rotation period at outer boundary of the disk. When  $M_* = 0.5M_\odot$ ,  $t = 10^3$  yr. The density wave will have a lifetime of order the orbital time scale, if no feedback or maintenance mechanism is included. The density wave exists longer if the effect of the ILR is avoided and the wave is amplified by some mechanisms (Bertin & Lin 1996). Short gaseous waves can propagate through the ILR all the way to the center, or through the OLR to infinity (Goldreich & Tremaine 1978, 1979). For a long wave, the ILR could be avoided if Toomre’s  $Q$  is sufficiently high in the central region, which acts as a  $Q$ -barrier to reflect the inward-traveling wave (Lin 1970). If a wave propagates outward and impinges on the corotation zone, it is subject to a turning-point effect, such that the wave evolves into a transmitted wave moving farther out and a stronger reflected wave moving back (overreflection; Mark 1974, 1976). The wave is thus amplified. With these assumptions, “quasi-stationary” spiral patterns can exist (Bertin & Lin 1996). Another possible scenario to maintain density waves is that they could act as a perturbation to excite the next generation of density waves, rendering density waves recurrent and similar to the GI-excited spiral arms in numerically simulated massive unstable disks (Tomida et al. 2017).

There have been many attempts to study GI-excited spiral arms using numerical simulations. It has been shown that disks can settle into a self-regulated state after several rotation periods, after heating by GI-induced dissipation balances cooling by self-radiation (Rice et al. 2003; Cossins et al. 2009; Rice & Armitage 2009; Forgan et al. 2011; Hall et al. 2019). Simulated spiral structures can also be recurrent, dissipating and then reforming on a time scale of several rotation periods (Nelson et al. 1998; Lodato & Rice 2005; Tomida et al. 2017). However, massive, early-type Class 0/I disks can be stabilized shortly after the envelope disperses and accretion from the envelope stops (Tomida et al. 2017).

#### 4.5. Caveats

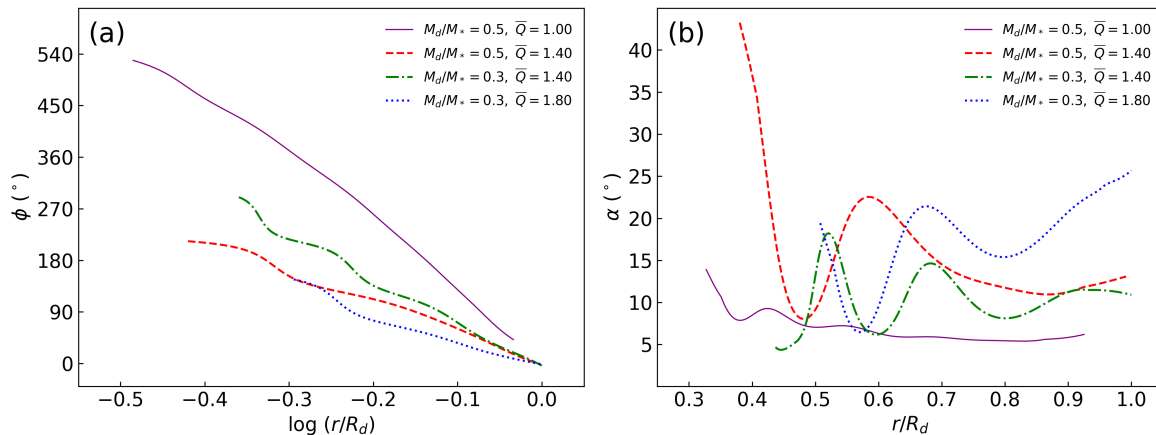


**Figure 7.** Spiral arms azimuthal angle ( $\phi$ ) and pitch angle ( $\alpha$ ) plotted as functions of radius. Results for Gaussian disks with  $(M_d/M_*, \bar{Q}) = (0.5, 1.00)$ ,  $(0.5, 1.40)$ ,  $(0.3, 1.40)$ , and  $(0.3, 1.80)$  are marked in purple solid, red dashed, green dashed-dotted, and blue dotted curves, respectively.

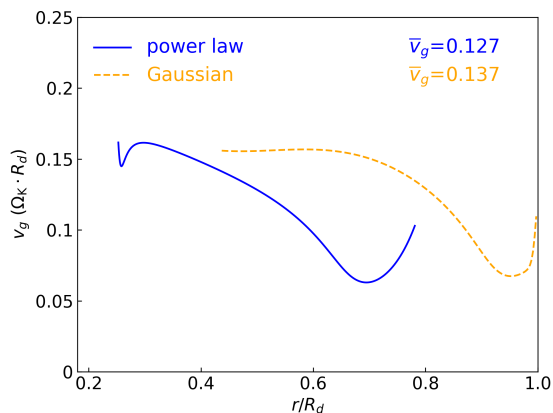


**Figure 8.** Group velocity of spiral density wave modes between inner and outer Lindblad radius. Blue solid and orange dashed curves mark the results in the fiducial power law and Gaussian disk, respectively. The average group velocity is shown at the upper-right corner.

This work focuses on  $m = 2$  modes, motivated by the prevalence of two-armed spirals in recent millimeter observations. In the context of the density wave theory, high-order ( $m > 2$ ) modes, having a narrower radial extent between the ILR and OLR, are more likely to be absorbed and therefore less likely to exist. If the conditions to avoid absorption are satisfied, high-order modes can occur and have higher growth rate to replace the  $m = 2$  mode. In our numerical calculations, the  $m = 2, 3, 4$  modes have a growth rate of 0.243, 0.422, 0.234 in the fiducial power law disk, and 0.242, 0.514, 0.571 in the fiducial Gaussian disk. Numerical simulations of self-gravitating disks have examined the dominant modes with  $m \approx M_*/M_d$  (Dong et al. 2015a; Hall et al. 2019), somewhat validating our choice of  $m = 2$  mode for the massive disks probed in this work. While low-mass disks are expected to have many arms, observations of systems

such as HD 100453 reveal two arms (Dong et al. 2016b), which might arise from the interaction between the disk and an embedded planet or external star. The nature of spiral arm number has yet to be explored thoroughly with the currently limited observations. Although we focus on  $m = 2$  modes, their general trends (Figure 6) will hold for high-order modes of multiple arms, should they exist, but with a systematic shift toward larger pitch angles as given by Equation (25).

We assume the protoplanetary disk to be razor-thin and analyze the disk dynamics in two dimensions, although the disks in our calculations have aspect ratio around 0.1. Neglecting disk thickness may influence the final results quantitatively, especially in potentially increasing the calculated pitch angle, as the finite thickness of a real disk dilutes the self-gravity (Kratte & Lodato 2016). Nevertheless, the qualitative physical trends presented in this work will not be adversely affected. In addition, limited to linear analysis, our model does not include shocks, viscosity, accretion, or saturation of wave modes. In the case of planet-excited spirals, the weakly non-linear analysis of Rafikov (2002) is consistent with the linear analysis and simulations by Zhu et al. (2015), while a new non-linear effect from massive planet is also reported. This suggests that the linear analysis can capture the key behavior of spiral arms, even if the complexities of protoplanetary disks require more detailed hydrodynamical simulations for more complete understanding.

## 5. SUMMARY

Spiral arms have been detected in protoplanetary disks (e.g., Hashimoto et al. 2011; Muto et al. 2012; Pérez et al. 2016; Andrews et al. 2018). An embedded planet or the gravitational instability can excite spiral arms. It has been shown that the pitch angle,

a quantity that describes the degree of arm winding, of planet-excited spiral wakes correlates with the disk sound speed, planet mass, and position of the planet (Rafikov 2002; Zhu et al. 2015; Zhang & Zhu 2020). However, the behavior of the spiral pitch angle of GI-excited density waves has not been explored. In this work, we calculate and analyze two-armed global spiral density wave modes in thin, non-viscous, self-gravitating protoplanetary disks under the dynamical effect of the gravity from the central star, disk self-gravity, and thermal pressure. We only consider massive ( $M_d/M_* \geq 0.1$ ), cool (Toomre  $\bar{Q} \leq 2$ ) disks, as low-mass hot systems are stable to non-axisymmetric spiral perturbation. Our disk models employ observationally motivated physical conditions, including both power law and Gaussian density profiles, a power law temperature profile, and three sets (reflecting, transmitting, and confining pressure) of boundary conditions. We probe the morphology of the resulting two-armed density wave modes and investigate the influence of the disk-to-star mass ratio ( $M_d/M_*$ ), average Toomre  $Q$  ( $\bar{Q}$ ), and average aspect ratio ( $\bar{h}$ ) on spiral pitch angle. Our main findings are:

1. The pitch angle and pattern speed of spiral density wave modes are insensitive to the boundary conditions adopted.
2. All else being equal, Gaussian disks possess more tightly wound spiral density waves than power law disks, suggesting that more evolved disks have more tightly wound spirals than less evolved disks.
3. At a fixed  $\bar{Q}$ , more massive disks, owing to their higher temperatures, have more loosely wound (more open) spirals.
4. At a fixed  $\bar{h}$ , more massive disks, owing to their higher self-gravity, have more tightly wound spirals.
5. At a fixed  $M_d/M_*$ , disks with higher  $\bar{Q}$  or  $\bar{h}$  have hotter temperatures and thus generate more loosely wound (more open) spirals.
6. The pitch angle scales with sound speed  $c_s$  and mass  $M_d$  of the disk as  $\alpha \propto c_s^2/M_d$ .
7. Unlike planet-launched spiral wakes, the amplitude of GI-excited spiral density waves fluctuates with radius, consistent with recent ALMA observations.
8. Unlike planet-launched spiral wakes, the radial variation of pitch angle of GI-excited density waves depends on  $c_s$  and  $M_d$ . The spiral pitch angle of massive cool disks decreases with increasing radius, while that of low-mass hot disks increases with radius.
9. Spiral density waves propagate at the group velocity on a time scale of a few rotation periods, suggesting that density waves need to be constantly replenished.

Comparison of our derived behavior of spiral amplitude and pitch angle with observations potentially can test the GI-excited density wave mechanism and constrain the properties of protoplanetary disks.

## ACKNOWLEDGMENTS

We acknowledge helpful discussions with Wing-Kit Lee, Zhaohuan Zhu, and Shangjia Zhang. We also thank the referee Ruobing Dong for helpful feedback. This work was supported by the National Science Foundation of China (11721303, 11991052) and the National Key R&D Program of China (2016YFA0400702).

## APPENDIX

### A. NUMERICAL PROCESS

We follow the numerical method described in Adams et al. (1989) to solve the integro-differential equation (Equation 13). We summarize the procedure below. After setting radial grid points on a logarithmic scale, we discretize the integro-differential equation and boundary conditions into matrix form, which gives  $\mathcal{W}(\omega)\mathbf{S} = 0$ . Equation (13) corresponds to the middle rows of  $\mathcal{W}(\omega)$ , and the inner and outer boundary condition correspond to the first and last row, respectively.

Equation (13) is transformed into

$$\begin{aligned}
(\mathcal{W}_g)_{ik} = & \nu(1 - \nu^2) \left\{ \mathcal{D}_{ij}^{(2)} + \left( Ar + 1 + \frac{2r}{\sigma_0} \frac{d\sigma_0}{dr} \right) \mathcal{D}_{ij}^{(1)} + \left[ Ar \left( 1 + \frac{r}{\sigma_0} \frac{d\sigma_0}{dr} \right) + Br^2 + \frac{r^2}{\sigma_0} \frac{d^2\sigma_0}{dr^2} + \frac{2r}{\sigma_0} \frac{d\sigma_0}{dr} \right] \delta_{ij} \right\} \mathcal{I}_{jk} \\
& + \frac{c_s^2 \nu (1 - \nu^2)}{2\pi G \sigma_0 r} \left\{ \mathcal{D}_{ik}^{(2)} + \left[ Ar + \frac{2r}{c_s^2} \frac{d(c_s^2)}{dr} - 1 \right] \mathcal{D}_{ik}^{(1)} + \left[ \frac{r^2}{c_s^2} \frac{d^2(c_s^2)}{dr^2} + Ar \frac{r}{c_s^2} \frac{d(c_s^2)}{dr} + Br^2 \right] \delta_{ik} \right\} - \left[ \frac{\kappa^2 \nu (1 - \nu^2)^2 r}{2\pi G \sigma_0} \right] \delta_{ik},
\end{aligned} \tag{A1}$$

where  $\mathcal{W}_g$  is an  $(N - 2) \times N$  matrix.  $\mathcal{D}^{(1)}$  and  $\mathcal{D}^{(2)}$  are the first and second order derivation operator, while  $\mathcal{I}$  is the disk self-gravity potential integration in matrix form. The matrix forms of the reflecting (Equation A2), transmitting (Equation A3), and confining pressure (Equation A4) boundaries read as:

$$\begin{aligned}
(\mathcal{W}_r)_{ik} = & \left\{ (\omega - m\Omega) \mathcal{D}_{ij}^{(1)} + \left[ (\omega - m\Omega) \left( \frac{r}{\sigma_0} \frac{d\sigma_0}{dr} + 1 \right) - 2m\Omega \right] \delta_{ij} \right\} \mathcal{I}_{jk} \\
& + \frac{c_s^2}{2\pi G \sigma_0 r} \left\{ (\omega - m\Omega) \mathcal{D}_{ik}^{(1)} + \left[ (\omega - m\Omega) \frac{r}{c_s^2} \frac{d(c_s^2)}{dr} - 2m\Omega \right] \delta_{ik} \right\},
\end{aligned} \tag{A2}$$

$$(\mathcal{W}_t)_{ik} = \mathcal{D}_{ik}^{(1)} + r \left( \frac{1}{\sigma_0} \frac{d\sigma_0}{dr} + i|k| \right) \delta_{ik}, \tag{A3a}$$

$$|k| = \frac{\pi G \sigma_0}{c_s^2} + \frac{\pi G \sigma_0}{c_s^2} [1 - Q^2 (1 - m^2)]^{1/2} \quad (\text{inner boundary : } \omega \ll \Omega, \kappa \simeq \Omega), \tag{A3b}$$

$$|k| = \frac{\pi G \sigma_0}{c_s^2} \left( 1 - \frac{Qm\Omega}{\kappa} \right) + \frac{\pi G \sigma_0 Q}{c_s^2} \omega \quad (\text{outer boundary : } Q \approx 1), \tag{A3c}$$

$$\begin{aligned}
(\mathcal{W}_c)_{ik} = & \left\{ (\omega - m\Omega) \mathcal{D}_{ij}^{(1)} + \left[ (\omega - m\Omega) \left( \frac{r}{\sigma_0} \frac{d\sigma_0}{dr} + 1 \right) - 2m\Omega \right] \delta_{ij} \right\} \mathcal{I}_{jk} \\
& + \frac{c_s^2}{2\pi G \sigma_0 r} \left\{ (\omega - m\Omega) \mathcal{D}_{ik}^{(1)} + \left[ (\omega - m\Omega) \frac{r}{c_s^2} \frac{d(c_s^2)}{dr} - 2m\Omega \right] \delta_{ik} \right\} - \frac{\kappa^2 (1 - \nu^2)}{2\pi G d\sigma_0 / dr} (\omega - m\Omega) \delta_{ik}.
\end{aligned} \tag{A4}$$

Note that we have made approximations on the wave number  $|k|$  of the transmitting boundary, in order for the resulting matrix be of integral order  $\omega$ . To transform Equation (22) into Equation (23), we analytically rewrite  $\mathcal{W}(\omega)$  into a fifth-order polynomial of  $\omega$ , and so Equation (22) becomes

$$[\mathcal{W}^{(5)} \omega^5 + \mathcal{W}^{(4)} \omega^4 + \mathcal{W}^{(3)} \omega^3 + \mathcal{W}^{(2)} \omega^2 + \mathcal{W}^{(1)} \omega + \mathcal{W}^{(0)}] \mathbf{S} = 0. \tag{A5}$$

By defining the  $5N$ -dimensional vector  $\mathbf{S}_d(\mathbf{S}, \omega)$ , we rewrite Equation (A5) into Equation (23), in which  $\mathcal{T}$  and  $\mathcal{Z}$  consist of polynomial coefficients  $\mathcal{W}^{(0)}, \mathcal{W}^{(1)}, \dots, \mathcal{W}^{(5)}$ . Their expressions can be found in Appendix B of Adams et al. (1989).

We use a softened gravity to deal with the singularity that arises in the potential integration (Section 2.3). The softening parameter  $\eta$  should not be too large, which would make the result deviate from real gravity, or too small, which would introduce large numerical errors. We have tested the influence of  $\eta$  on the calculated density wave modes and adopted an appropriate value. For example, for our fiducial power law disk, we use  $\eta_1^2 = 10^{-2}$  for  $\Omega$  (a relatively large  $\eta$  to assure that the  $\Omega$  and  $\kappa$  curves are smooth), and we set  $\eta_2^2 = 10^{-5}$  for  $\Psi_1$ . When we change  $\eta_2^2$  to  $10^{-7}$ , the resulting growth rate changes from 0.243 to 0.223; thus, the softening parameters we chose lie in the convergence region. We have also tested the effect of the number of grid points ( $N$ ) on our results. In the fiducial Gaussian disk, calculation with  $N = 500$  results in  $\omega = 1.57 - 0.242i$ , while that with  $N = 1000$  gives almost the same result,  $\omega = 1.57 - 0.245i$ . We thus adopt  $N = 500$  to improve calculation efficiency.

To test the validity of our numerical processing, we reproduce a representative mode in Adams et al. (1989) (Figure A1). Our calculated wave frequency ( $\omega = 4.11 - 0.217i$ ) is well consistent with their result ( $\omega = 4.26 - 0.232i$ ), with a difference of only  $\sim 5\%$ . Our perturbation density  $S(r)$  is also in excellent agreement with Adams et al. (1989, see their Figure 3). The small difference between the results comes from the different methods we use in calculating  $\Omega$  and dealing with the singularity.

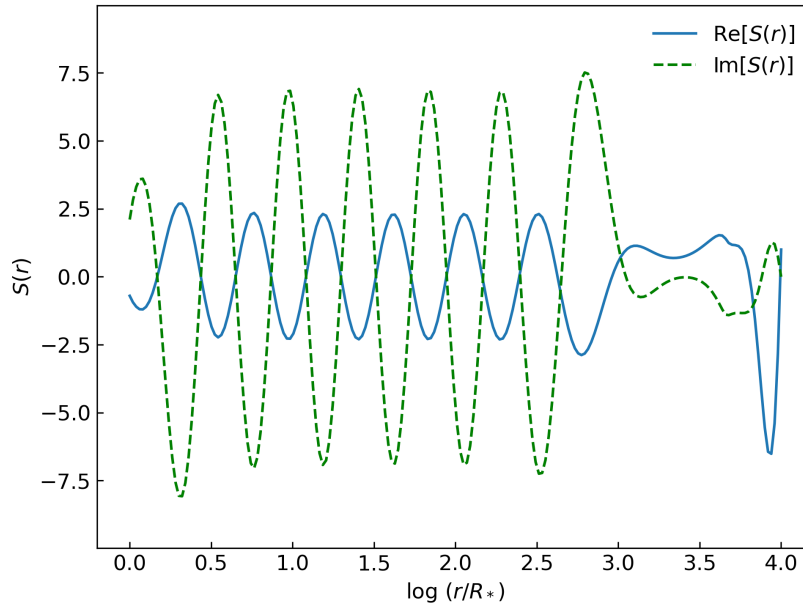


**Figure A1.** Reproduction of Figure 3 of Adams et al. (1989). This plot is the non-dimensional perturbation density distribution  $S(r) = \sigma_1(r)/\sigma_0(r)$  of the lowest mode in the fiducial disk of Adams et al. (1989). The blue solid line shows the real part of the function, and the green dashed line shows the imaginary part of the function.

#### REFERENCES

- Adams, F. C., Ruden, S. P., & Shu, F. H. 1989, *ApJ*, 347, 959
- ALMA Partnership, Brogan, C. L., Pérez, L. M., et al. 2015, *ApJL*, 808, L3
- Andrews, S. M., Huang, J., Pérez, L. M., et al. 2018, *ApJL*, 869, L41
- Andrews, S. M., Rosenfeld, K. A., Kraus, A. L., et al. 2013, *ApJ*, 771, 129
- Andrews, S. M., Wilner, D. J., Espaillat, C., et al. 2011, *ApJ*, 732, 42
- Andrews, S. M., Wilner, D. J., Hughes, A. M., et al. 2009, *ApJ*, 700, 1502
- Avenhaus, H., Quanz, S. P., Schmid, H. M., et al. 2017, *AJ*, 154, 33
- Bae, J., & Zhu, Z. 2018, *ApJ*, 859, 118
- Benisty, M., Juhasz, A., Boccaletti, A., et al. 2015, *A&A*, 578, L6
- Benisty, M., Stolker, T., Pohl, A., et al. 2017, *A&A*, 597, A42
- Bertin, G. & Lin, C. C. 1996, *Spiral Structure in Galaxies: A Density Wave Theory* (Cambridge, MA: MIT Press)
- Bertin, G., Lin, C. C., Lowe, S. A., et al. 1989, *ApJ*, 338, 78
- Binney, J., & Tremaine, S. 2008, *Galactic Dynamics, Second Edition* (Princeton: Princeton Univ. Press)
- Boehler, Y., Weaver, E., Isella, A., et al. 2017, *ApJ*, 840, 60
- Canovas, H., Montesinos, B., Schreiber, M. R., et al. 2018, *A&A*, 610, A13
- Chiang, E. I. & Goldreich, P. 1997, *ApJ*, 490, 368
- Cossins, P., Lodato, G., & Clarke, C. J. 2009, *MNRAS*, 393, 1157
- Dipierro, G., Lodato, G., Testi, L., et al. 2014, *MNRAS*, 444, 1919
- Dipierro, G., Pinilla, P., Lodato, G., et al. 2015, *MNRAS*, 451, 974
- Dong, R., Hall, C., Rice, K., et al. 2015a, *ApJL*, 812, L32
- Dong, R., Liu, S.-Y., Eisner, J., et al. 2018a, *ApJ*, 860, 124
- Dong, R., Najita, J. R., & Brittain, S. 2018b, *ApJ*, 862, 103
- Dong, R., Vorobyov, E., Pavlyuchenkov, Y., et al. 2016a, *ApJ*, 823, 141
- Dong, R., Zhu, Z., Fung, J., et al. 2016b, *ApJL*, 816, L12
- Dong, R., Zhu, Z., Rafikov, R. R., et al. 2015b, *ApJL*, 809, L5
- Dullemond, C. P., Isella, A., Andrews, S. M., et al. 2020, *A&A*, 633, A137
- Feng, C.-C., Lin, L.-H., Wang, H.-H., et al. 2014, *ApJ*, 785, 103
- Forgan, D. H., Ilee, J. D., & Meru, F. 2018, *ApJL*, 860, L5
- Forgan, D., Rice, K., Cossins, P., et al. 2011, *MNRAS*, 410, 994
- Fung, J., & Dong, R. 2015, *ApJL*, 815, L21
- Garufi, A., Quanz, S. P., Avenhaus, H., et al. 2013, *A&A*, 560, A105
- Goodman, J. & Rafikov, R. R. 2001, *ApJ*, 552, 793
- Goldreich, P., & Tremaine, S. 1978, *ApJ*, 222, 850



- Goldreich, P., & Tremaine, S. 1979, *ApJ*, 233, 857
- Grady, C. A., Muto, T., Hashimoto, J., et al. 2013, *ApJ*, 762, 48
- Hall, C., Dong, R., Rice, K., et al. 2019, *ApJ*, 871, 228
- Hall, C., Rice, K., Dipierro, G., et al. 2018, *MNRAS*, 477, 1004
- Hashimoto, J., Tamura, M., Muto, T., et al. 2011, *ApJL*, 729, L17
- Huang, J., Andrews, S. M., Öberg, K. I., et al. 2020, *ApJ*, 898, 140
- Huang, J., Andrews, S. M., Pérez, L. M., et al. 2018, *ApJL*, 869, L43
- Kratter, K., & Lodato, G. 2016, *ARA&A*, 54, 271
- Kurtovic, N. T., Pérez, L. M., Benisty, M., et al. 2018, *ApJL*, 869, L44
- Laughlin, G., & Bodenheimer, P. 1994, *ApJ*, 436, 335
- Laughlin, G., & Korchagin, V. 1996, *ApJ*, 460, 855
- Laughlin, G., Korchagin, V., & Adams, F. C. 1997, *ApJ*, 477, 410
- Laughlin, G., Korchagin, V., & Adams, F. C. 1998, *ApJ*, 504, 945
- Laughlin, G., & Rozyczka, M. 1996, *ApJ*, 456, 279
- Lee, W.-K., Dempsey, A. M., & Lithwick, Y. 2019, *ApJ*, 872, 184
- Lin, C. C. 1970, in *IAU Symp. 38: The Spiral Structure of our Galaxy*, ed. E. Becker & G. I. Kontopoulos (Dordrecht: Reidel), 377
- Lin, C. C., & Shu, F. H. 1964, *ApJ*, 140, 646
- Lin, M.-K. 2015, *MNRAS*, 448, 3806
- Lodato, G., & Rice, W. K. M. 2005, *MNRAS*, 358, 1489
- Lynden-Bell, D. & Kalnajs, A. J. 1972, *MNRAS*, 157, 1
- Mark, J. W. K. 1974, *ApJ*, 193, 539
- Mark, J. W. K. 1976, *ApJ*, 205, 363
- Meru, F., Juhász, A., Ilee, J. D., et al. 2017, *ApJL*, 839, L24
- Miranda, R., & Rafikov, R. R. 2019, *ApJ*, 875, 37
- Muto, T., Grady, C. A., Hashimoto, J., et al. 2012, *ApJL*, 748, L22
- Nelson, A. F., Benz, W., Adams, F. C., et al. 1998, *ApJ*, 502, 342
- Noh, H., Vishniac, E. T., & Cochran, W. D. 1991, *ApJ*, 383, 372
- Papaloizou, J. C. B. 2002, *A&A*, 388, 615
- Papaloizou, J. C. B., & Lin, D. N. C. 1989, *ApJ*, 344, 645
- Papaloizou, J. C., & Savonije, G. J. 1991, *MNRAS*, 248, 353
- Pérez, L. M., Carpenter, J. M., Andrews, S. M., et al. 2016, *Science*, 353, 1519
- Pérez, L. M., Carpenter, J. M., Chandler, C. J., et al. 2012, *ApJL*, 760, L17
- Piétu, V., Dutrey, A., Guilloteau, S., et al. 2006, *A&A*, 460, L43
- Pinilla, P., Tazzari, M., Pascucci, I., et al. 2018, *ApJ*, 859, 32
- Rafikov, R. R. 2002, *ApJ*, 569, 997
- Rice, W. K. M., & Armitage, P. J. 2009, *MNRAS*, 396, 2228
- Rice, W. K. M., Armitage, P. J., Bate, M. R., et al. 2003, *MNRAS*, 339, 1025
- Shu, F. H. 2016, *ARA&A*, 54, 667
- Tang, Y.-W., Guilloteau, S., Piétu, V., et al. 2012, *A&A*, 547, A84
- Tomida, K., Machida, M. N., Hosokawa, T., et al. 2017, *ApJL*, 835, L11
- Toomre, A. 1964, *ApJ*, 139, 1217
- Toomre, A. 1969, *ApJ*, 158, 899
- Tremaine, S. 2001, *AJ*, 121, 1776
- Uyama, T., Hashimoto, J., Muto, T., et al. 2018, *AJ*, 156, 63
- Wagner, K., Apai, D., Kasper, M., et al. 2015, *ApJL*, 813, L2
- Wagner, K., Dong, R., Sheehan, P., et al. 2018, *ApJ*, 854, 130
- Wilner, D. J., Ho, P. T. P., Kastner, J. H., et al. 2000, *ApJL*, 534, L101
- Yu, S.-Y., Ho, L. C., & Zhu, Z. 2019, *ApJL*, 877, 100
- Zhang, S. & Zhu, Z. 2020, *MNRAS*, 493, 2287
- Zhu, Z., Dong, R., Stone, J. M., et al. 2015, *ApJ*, 813, 88